Iraqi Journal of Physics, 2025
https://doi.org/10.30723/ijp.v23i4.1429

Vol.23, No.4, PP.143-158
P-ISSN: 2070-4003
E-ISSN: 2664-5548

Preparation and Characterization of Au/TiO_2:CdS Thin Film as Photocatalysis for Degradation of MB Dye in Water

Zainb K. Mohamed[1], Mahdi M. Mutter[2*] and Souad G. Khalil[1]

[1]*Department of Physics, College of Science for Women, University of Baghdad, Baghdad, Iraq*
[2]*Scientific Research Commission, Ministry of Higher Education & Scientific Research, Baghdad, Iraq*
[*]Corresponding author: mahdimutter@yahoo.com

Abstract

In this work, gold/ titanium oxide: cadmium sulfide (Au/TiO_2:CdS) thin film nanocomposites as photocatalysts were synthesized using the sol-gel technique and deposited on glass substrates using the dipping method for the degradation of Methylene Blue (MB) dye in water. The CdS doping with TiO2 at ratios 1:1, 0.25, and 0.5 wt%. Au/TiO_2: CdS thin film characterization was achieved using X-ray diffraction (XRD), atomic force microscopy (AFM), Raman spectroscopy, field effect electron scanning microscopy (FESEM), and UV-Vis spectroscopy. The results of XRD showed that the obtained phase of TiO_2: CdS was cubic. The results of AFM showed that the distribution of grain sizes increased with increasing CdS concentration, as did the roughness and RMS. The FESEM results indicated that the particle size decreased from 58.68 nm to 22.24 nm as the concentration of CdS increased. Raman spectroscopy revealed that the TiO_2 peaks appear only at 1300 cm^{-1} (B1g), 1600 cm^{-1} (A1g), and 2000 cm^{-1} (Eg). The optical properties were enhanced after the addition of CdS. The photocatalytic decomposition of Au/TiO_2: CdS thin films was investigated by the degradation of MB dye in water under ultraviolet (UV) light exposure. The results showed excellent photocatalytic performance after the addition of CdS.

Article Info.

Keywords:
Au/TiO_2, CdS Thin Films, Optical Properties, So-Gel Dipping, Raman Spectroscopy.

Article history:
Received: Jan. 31, 2025
Received: Apr. 26, 2025
Accepted: May,14,2025
Published:Dec.01,2025

1. Introduction

In the past decades, researchers have been interested in using photocatalysis in many chemical processes, especially in the field of environment, due to the urgent need to use environmentally friendly methods to get rid of pollutants, especially toxic organic compounds that pollute the air and water [1]. Titanium (IV) oxide (TiO_2) is one of the many photocatalysts that has drawn much interest in industrial applications because of its many benefits, including cheap cost, stability, and performance. TiO_2 photocatalytic performance is limited in some ways.

Since TiO_2 is primarily an n-type semiconductor with a broad band gap (anatase, energy gap (E_g) = 3.2 eV, and rutile, E_g = 3.0 eV), it can only be activated at UV wavelengths, which excites an electron from the valence band to the conduction band [2]. This indicates that TiO_2 can only be activated using 4-5% of the solar energy from sunshine [3]. To increase TiO_2 photo response to longer wavelengths, considerable efforts have been performed [4, 5]. However, some problems limited the significant expansion of its use in this field, such as the need to use an ultraviolet (UV) excitation source. To solve this problem, the light absorption range of titanium dioxide was expanded, and different methods were used [6].

Photons within the visible spectrum (400 nm to 750 nm) stimulate CdS, a photocatalyst. It is a dimeric semiconductor with a band gap of 2.4 eV and is a member of the II-VI group [7]. Unlike the more often used lower photocatalytic activity thresholds of 4% to 5%, CdS has a high photocatalytic activity that enables greater utilization of the solar spectrum, i.e., 40% to 50% [8]. Numerous techniques, including decorating titanium dioxide with metal nanoparticles

(NPs) [9, 10] and combining it with other semiconductor photocatalysts [11], have been documented to increase the absorption of titanium dioxide to visible wavelengths and to increase the lifetime of electron-hole pairs in titanium dioxide. Because of the noble metals' Localized Surface Plasmon Resonance (LSPR), decorating titanium dioxide with gold nanoparticles causes its activation wavelength to expand into the visible spectrum [12]. Researchers have used many combinations of heterojunctions (TiO_2: ZnO, SnO_2: TiO_2, and TiO_2: PbO) [13]. The overlay and doping between cadmium and titanium dioxide showed high photocatalytic efficiency as an effective photocatalyst for visible and ultraviolet light. Many researchers have studied the CdS/TiO_2 heterojunctions [14]. One approved method to improve the photocatalytic process in semiconductors is using plasmonic photocatalysts made of metals and semiconductors. The most important of these plasmonic materials are gold nanoparticles (Au NPs). Thin film of gold was deposited with a nano thickness as like island on the surface of the TiO_2: CdS films [15].

In this paper, the Au/ TiO_2:CdS thin films were synthesized for photocatalysis applications to eliminate pollutants from water, especially Methylene Blue (MB) dye. Its properties were investigated by X-ray diffraction (XRD), and Field Emission Scan Electronic Microscope (FESEM). The catalytic activity of the prepared films with different doping ratios in eliminating MD was also studied and analyzed.

2. Experimental Details

For the purpose of preparing Au/TiO_2:CdS thin film, the following materials were used: Tetra(ethyl)titanium oxyhydroxide ($TiOCH(CH_3)_4$), ethanol (C_2H_5O), acetic acid (CH_3COOH), polyethylene glycol, cadmium acetate, and thiourea. All the materials of 99% purity were purchased from Merch KGaA, Germany.

Au/TiO_2:CdS film was deposited using the sol-gel and the dipping methods at 0.5 M of all solution prepared. First, CdS solution was prepared by dissolving 0.1072 g of cadmium diacetate dihydrate ($Cd(Ac)_2.2H_2O$) in 25 ml of ethylene glycol with stirring at 60 °C. 0.006 g of thiourea was diluted in 12.5 mL of ethylene glycol and added dropwise with continuous stirring for 1 hour to the CdS solution. Second, TiO_2 solution was prepared by dissolving 3.15 mL of $TiOCH(CH_3)_4$ in 25 mL of ethanol and 5 mL of acetic acid with continuous stirring for an hour. Thirdly, the TiO_2:CdS was prepared by mixing the two prepared solutions with different doping ratios of cadmium sulphate (1, 0.25, and 0.5) wt% using the sol-gel method. To prepare the TiO_2:CdS thin films, the TiO_2:CdS solution was deposited on glass substrates by the dipping method at a dipping speed of 1 cm/s. After each dipping process, the sample was dried using an oven at a temperature of 100 °C for 15 minutes. The dipping process was repeated 3 times to obtain the desired thickness. Finally, using a Prothero oven, the films were heated at 500 °C for 4 hours in air. The thicknesses were determined using a device of the type (Stellar Net pp2000), it measures thickness using the fringes interference method and calculates thickness values using software via a computer specific to the device. The measured thicknesses were 286.9, 1110.6, 729, and 379.6 nm for TiO_2:CdS, TiO_2:0.25%CdS, and TiO_2:0.5%CdS thin films, respectively. The TiO_2:CdS thin films were placed inside a plasma sputtering chamber to deposit gold as like islands on the prepared film surfaces. The chamber was evacuated to 3×10^{-5} Torr [15], and the distance between the target and the sputtering electrode was 5 cm. Argon gas was used, with a flow rate of 27 cm^3/min and a working pressure of 4×10^{-2} Torr. To increase the homogeneity in the bound site of the thin films, the substrate was gradually heated to a balanced temperature of 200 °C while rotating it during deposition. The gold deposited on the surface of the thin film was in 5 island-like shapes with 3 mm diameters for each one.

2 .1. The Photocatalytic Activity Process

To ascertain the photocatalytic activity of the synthesized TiO_2:CdS thin films, the degradation of MB dye was evaluated. This was performed in an aqueous solution containing the Au/TiO_2:CdS thin film under UV light irradiation. For each experiment, 50 mL of a 5 mg/L MB aqueous solution was introduced into a circular glass jar with a diameter of 4.5 cm. The solution of MB dye was then stirred for 30 minutes at room temperature in the dark to establish adsorption-desorption equilibrium. To assess their impact, the prepared samples were deposited onto 10×10 mm^2 glass slide substrates. During the photocatalytic activity, the glass vessel holding the MB dye solution was exposed to the environment and kept in an ice bath to maintain a steady temperature. The MB dye was exposed to UV light using a 300 W tungsten lamp (Philips halogen) with a cutoff filter ($\lambda > 420$ nm); the lamp was positioned 20cm away from the solution surface. On exposure to the UV light, the concentration of MB dye in the aqueous solution decreased as a result of the dye's adsorption onto the Au/TiO_2:CdS film surface. The dye absorbance following UV irradiation for different periods 10 to 80 minutes was measured using a Shimadzu UV-16001 UV-visible spectrometer. The absorbance of the MB dye solutions, i.e. the dye content, was altered by this adsorption. To remove the background effect, the photoinduced responses were observed after the synthesized TiO_2:CdS thin films were left in the MB dye solution for 30 minutes in the dark.

The relationship between absorbance (A) and the Methylene Blue (MB) dye concentration (Δ) at time t is expressed by the following equation [16]

$$C = A_o/A \quad \textbf{(1)}$$

where C is concentration of MB dye, A_o is the absorbance of MB before irradiation, and A is the absorbance of MB after irradiation.

2 .2. Mechanism of Degradation

Eqs. (2-4) describe the beginning of the mechanisms. Eq. (5) describes the formation of a superoxide radical anion ($O_2\cdot$) by oxygen adsorption, whereas Eq. (6) describes the formation of hydrogen peroxide (H_2O_2), which in turn produces a hydroxyl radical ($\cdot OH$) (Eq. (7)). Both surface and solution pollutants will be attacked by these produced radicals (Eq. (8)). This action increases the quantity of oxygen radicals that will attack the pollutants by preventing this electron from recombining with the hole (106, 107). The following is a description of these reactions [16]:

$$TiO_2 + h\nu \leftrightarrow TiO_2(h^+ + e^-) \quad \textbf{(2)}$$
$$TiO_2(h^+ + e^-) + H_2O_{adsorbed} \leftrightarrow TiO_2(e^-) + H^+ + \cdot OH \quad \textbf{(3)}$$
$$h^+ + OH^-_{adsorbed} \leftrightarrow \cdot OH \quad \textbf{(4)}$$
$$e^- + O_2 \rightarrow O\cdot_2^- \quad \textbf{(5)}$$
$$2e^- + O_2 + 2H^+ \rightarrow H_2O_2 \quad \textbf{(6)}$$
$$H_2O_2 + O\cdot_2^- \rightarrow \cdot OH + OH^- + O_2 \quad \textbf{(7)}$$
$$\cdot OH + dye \rightarrow degradation\ products \quad \textbf{(8)}$$

2 .3. Characterization

XRD patterns were used to describe the structural property of the TiO_2:CdS thin films, an X-ray diffractometer type the Bruker D8 ADVANCE with CuKα_1 (made in the U.S.) was used. A UV-Vis spectrophotometer (Shimadzu UV-16001) was used to investigate the optical properties. The FESEM (type JEOL, JSM-67001), and Atomic Force Microscope (AFM) type Bruker MultiMode 8-HR AFM, made in USA were also used to characterize the prepared thin films.

2. Results

Fig. 1 shows the XRD patterns of the pure TiO_2, TiO_2:CdS and TiO_2:(0.5, 0.25) wt% CdS films. Analysis of the results of pure TiO_2 revealed that the peaks observed belonged only to the anatase phase. The anatase phase of TiO_2 (JCPDS No. 21-1272) is responsible for the diffraction peaks observed at 2θ angles of 25.042°, 37.904°, 48.011°, and 62.762°, which are consistent with the (101), (004), (200), and (204) crystal phases, respectively [16], as shown in Fig. 1a. The diffraction peaks matched a crystal structure of anatase TiO_2.

The TiO_2:(0.5, 0.25) wt% CdS and TiO_2:CdS(1:1) XRD patterns, Fig. 1(b, c, d), have diffraction peaks corresponding to CdS at angles of 23.01°, 35.274°, 55.73°for the (101), (102), (201) planes, respectively, according to the JCPDS cart. No. 41-1049. The anatase peak of TiO_2 coincided with the peak at 25.042°, attributed to CdS. In addition, a small peak was observed in other samples of TiO_2:CdS and TiO_2:0.25%wt CdS. The formation of a peak at 23.536° in the composites indicated the presence of a cubic phase of CdS [17]. The XRD patterns showed no additional peaks, indicating that only pure phases of titanium dioxide and cadmium sulphide were formed. As the concentration of cadmium sulphide increased, the peaks associated with cadmium sulphide became more pronounced.

XRD measurements indicated that the samples exhibited a high degree of crystallinity. The nanocomposites showed an anatase phase for the titanium dioxide component and a cubic phase for the cadmium sulphide component. The Scherrer's formula (Eq. (9)) was used to determine the average crystalline size (D) in nm [18]:

$$D = \frac{0.9\lambda}{\beta\cos\theta} \quad (\mathbf{9})$$

where D is the average crystallite size (in nm), λ is the X-ray wavelength of 1.54 °A, k is the Scherrer constant equal to 0.89, θ is the diffraction angle, and β is the full width at half maximum (FWHM) (in radian). The results indicated that the average crystallite size of pure titanium dioxide film was 11.75 nm, while the particle sizes of TiO_2:CdS(1:1) and TiO_2: (0.5, and 0.25) wt% CdS films were (8.25, 14.16, and 13.33) nm, respectively, as shown in Table 1. Dislocation density ($\boldsymbol{\delta}$) and macrostrain ($\boldsymbol{\varepsilon}$) were determined by Eqs. (10 and 11) [19]:

$$\delta = \frac{1}{D_2} \quad \mathbf{(10)}$$

$$\epsilon = \frac{\beta\cos\theta - \frac{\kappa\lambda}{D}}{4\sin\theta} \quad (\mathbf{11})$$

where δ represents the dislocation density line/nm^2, ϵ represents macrostrain.

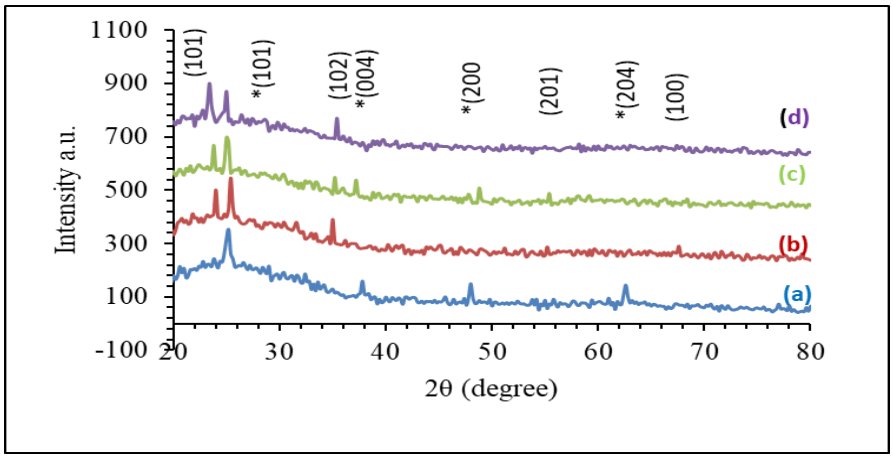

Figure 1: XRD patterns of (a) TiO_2 pure, (b) 0.25wt% CdS, (c) 0.5wt% CdS, (d) TiO_2:CdS(1:1).

Table 1: The parameters of XRD of TiO_2 and TiO_2: CdS films.

samples	2θ	d (nm)	FWHM	Crystalline D (nm)	Dislocation δ line/nm	β	θ	ε
TiO_2	25.042	0.3553	0.685	13	0.00591	0.01194	12.521	0.0658
	37.904	0.23717	1.026	9	0.01234	0.01789	18.952	0.043525
	48.011	0.18934	0.507	18	0.00308	0.00884	24.005	0.00105
	62.262	0.14792	1.4	7	0.02040	0.02442	31.381	0.17474
TiO_2:CdS	23.536	0.37768	1.011	8	0.01562	0.01763	11.768	-0.0043
	25.403	0.35034	1.134	7	0.02040	0.01978	12.701	0.036375
	36.464	0.2462	0.846	10	0.01	0.01475	18.232	-0.00519
	67.743	0.13821	1.26	8	0.01562	0.02198	33.871	-0.00671
TiO_2:0.5 %CdS	24.988	0.35606	0.49	18	0.00308	0.00854	12.494	-0.02948
	27.485	0.32425	0.4	22	0.00206	0.00697	13.742	0.000727
	35.972	0.24945	1.098	8	0.01562	0.01915	17.986	-0.00409
	39.395	0.22853	1.112	8	0.01562	0.01939	19.697	0.004278
	47.728	0.1904	0.564	17	0.00346	0.00983	23.864	-0.00077
	54.309	0.16878	0.787	12	0.00694	0.01372	27.154	-0.00166
TiO_2:0.25 CdS	23.75	0.37433	0.954	9	0.01234	0.01664	11.875	-0.00503
	25.51	0.35574	0.538	16	0.00390	0.00938	12.505	-0.03818
	36.379	0.24676	0.615	15	0.00444	0.01072	18.189	-0.00346

Fig. 2 illustrates the relationship between the size of the crystals and the amount of CdS present. The findings indicated that the size of the crystals grew as the CdS content increased at 0.25% and 0.5% from 13.33 to 14.16 nm but dropped at TiO_2(1:1) CdS sample where it reached 8.25 nm. The variation in ionic radius of Cd ion, Ti ion, and S ion were (151, 134, and 105) pm, respectively, responsible for the observed phenomenon. The crystallite size was

observed to increase with the addition of cadmium sulfate from 0.25 to 0.5 weight percentage. However, at a 1:1 TiO_2:CdS molar ratio, a decrease in crystallite size was noted, which can be attributed to the disparity in atomic radii [20].

Fig. 3 illustrates the correlation between dislocation density, macrostrain, and the concentration of CdS. Initially, the dislocation density was relatively low at 0.0068 line/nm for the 0.25 wt% CdS sample, subsequently increasing to 0.01541 line/nm in the 1:1 TiO_2:CdS sample. This trend is attributed to the discrepancy in ionic radii among Cd, Ti, and S, in conjunction with the influence of CdS on the Au/TiO_2 composite. Similarly, the macrostrain exhibited an initial low value of 0.00565 at 0.5 wt% CdS, which then increased to 0.0131 in the 1:1 TiO_2:CdS sample. These observations are consistent with the findings of Sharma et al. [20]. Furthermore, the obtained XRD results for Au/TiO_2:CdS align with those reported by Aoudjt et al. [21].

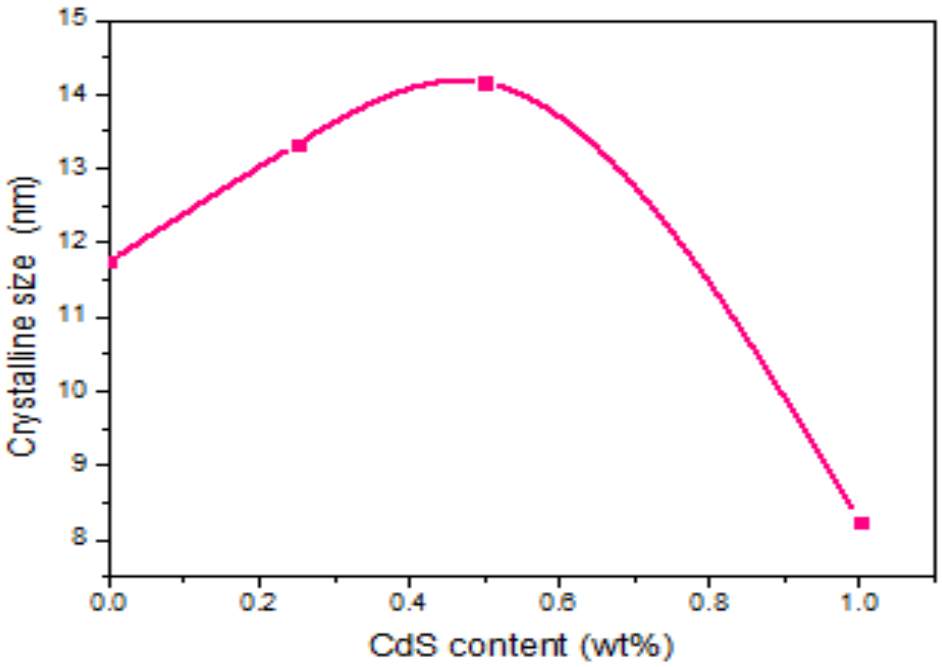

Figure 2: The crystalline size of TiO_2:CdS vs CdS concentration.

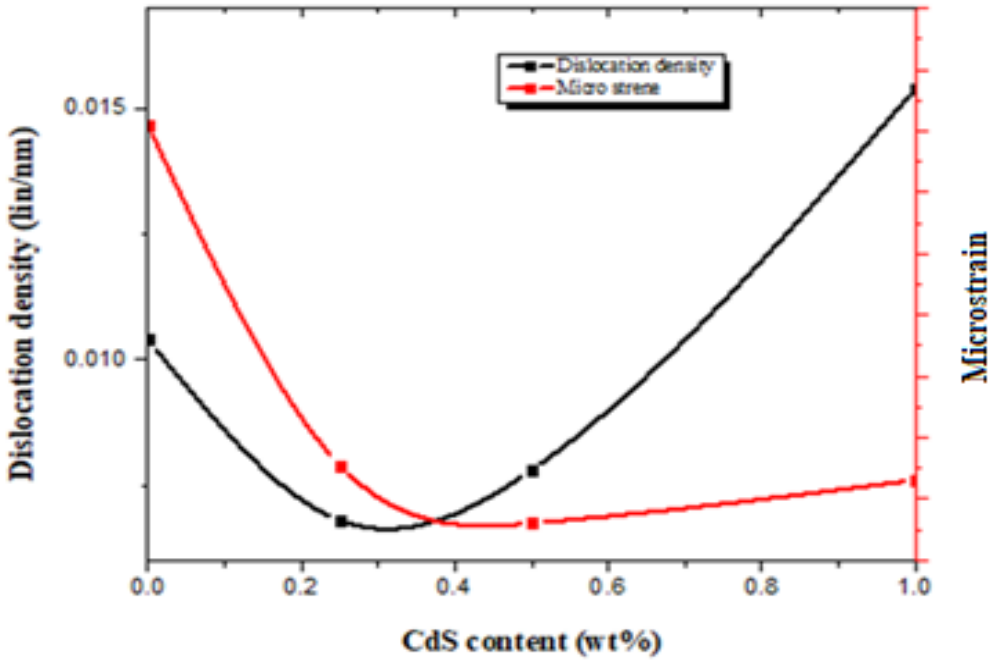

Figure 3: Macrostrain and dislocation density of TiO_2:CdS vs CdS concentration.

Fig. 4 shows 3D AFM images of TiO_2 and TiO_2:CdS thin films deposited using the sol-gel and dipping method. Table 2 shows the values of the grain size surface distribution, roughness of the films (R), the root mean square (RMS), and the particle density. The results showed that the grain size distribution on the surface of the prepared films increased from 25.65 nm to 53.77 nm as the percentage of CdS increased. As for the (1:1) sample, the grain size surface distribution decreased to 26.70 nm, but it remained more than the TiO_2 pure sample. The reason can be attributed to the difference in the atomic size of the cadmium, sulfur, and titanium ions [22]. The results also showed that the density of the particles increased in the TiO_2:0.25wt% CdS film to 5.13 nm, and this was due to the difference in ionic size between the elements that make up the density of the thin films, where the size of the titanium ion is larger. Increasing the CdS content led to a greater void volume within the thin film due to enhanced particle stacking, which subsequently reduced the particle density. This decrease in density was observed with increasing CdS content up to 0.5 wt% and a 1:1 molar ratio. Furthermore, Table 2 indicates that both roughness and average grain size increased from 5.13 nm to 5.74 nm as the CdS percentage rose. However, these values subsequently decreased to 5.13 nm in the 1:1 sample. The RMS increased from 6.63 to 8.25 nm with increasing CdS percentage. The images showed uniformity in the distribution of particles on the surface in terms of roughness, which is important in optical, sensing, and photocatalytic applications because it provides a larger surface area for reaction [23]. The obtained results from images of AFM outcomes concur with the results of Zhou et al. [24].

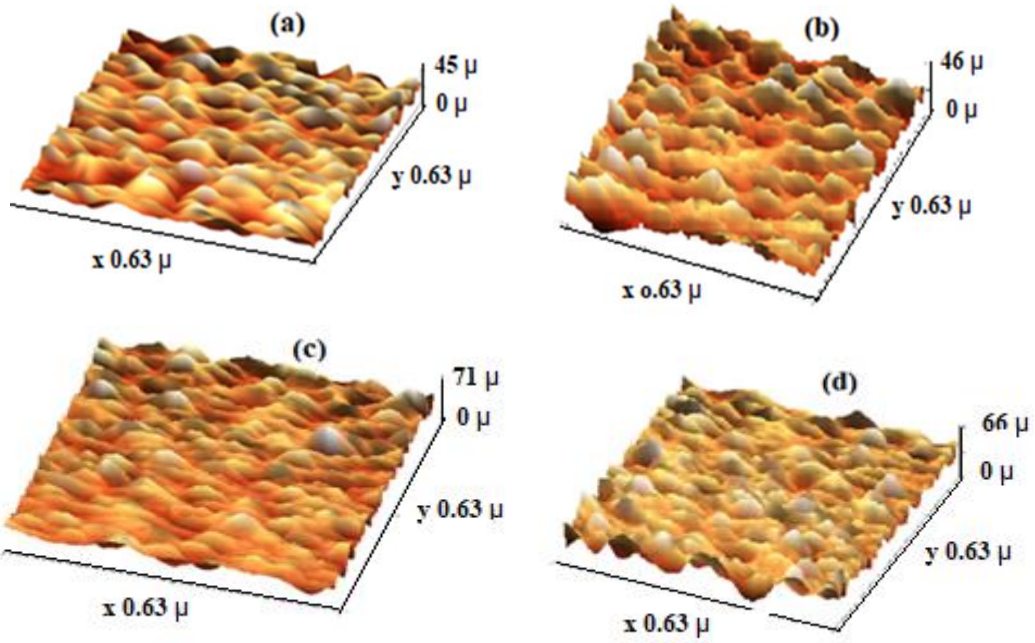

Figure 4: 3D AFM images of Au/TiO_2: CdS, (a) TiO_2 pure, (b) TiO_2(1:1) CdS, (c) TiO_2:0.5wt%Cds, (d) TiO_2:0.25wt%CdS.

Table 2: The parameters of the atomic force microscope images of the Au/TiO_2: CdS.

Samples	Average of grain size distribution (nm)	Roughness (nm)	RMS (nm)
TiO_2	25.65	5.13	6.63
TiO_2:0.25wt%Cds	37.85	5.61	7.69
TiO_2:0.5wt%CdS	53.77	5.74	8.25
TiO_2(1:1)CdS	26.70	5.13	6.53

Fig. 5 showed FESEM images which display the sizes, forms, and morphologies of TiO_2, TiO_2 (1:1) CdS and with different content of CdS (0.25 wt%, 0.5 wt%) thin films. The results showed that the particle sizes were about 58.68, 29.74, 26.15, and 22.24 nm of TiO_2:(0, 0.25, 0.5, and 1:1) CdS, respectively. Clumping was seen, and the images showed excellent dispersion. These results are consistent with the findings of Cerdán-Pasarán et al. (2019) [25]. The different concentrations of sol-gel solution during the preparation of Au/TiO_2:CdS thin films may account for this phenomenon.

It has been shown that increasing the concentration of TiO_2 and TiO_2:CdS thin films may induce alterations in the morphology of nanoparticles. Revathi et al. [26] suggested that agglomeration may alter the morphology of nanoparticles.

.

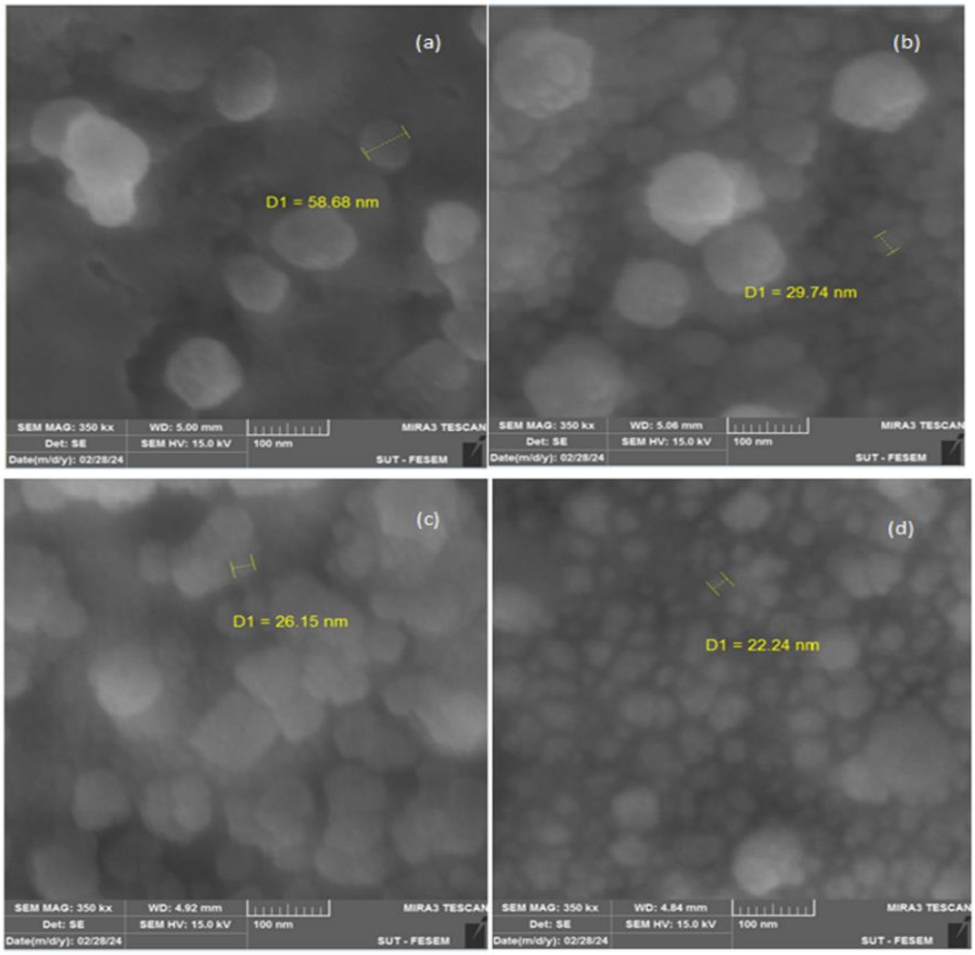

Figure 5: FESEM images of TiO_2 and TiO_2: CdS thin films.

The energy shift caused by the incorporation of CdS into TiO_2 and the variations in the Raman bands of TiO_2 thin films were shown by Raman spectroscopic studies (Fig. 6). The character table of the D4h point group, which primarily considers the anatase form of TiO_2, revealed that anatase contains six Raman active modes (A1g, 2B1g, and 3Eg). The spectra showed typical peaks of Longitudinal Optical (LO) modes, the first tone of which was at 150 cm^{-1} of TiO_2. Fig. 6 makes it evident that only the 1300 cm^{-1} (B1g), 1600 cm^{-1} (A1g), and 2000 cm^{-1} (Eg) peaks for TiO_2 appear [27]. Consequently, after adding CdS to the TiO_2 matrix, a noticeable peak shift (blue shift) from 150 to 140 cm^{-1} was identified [28]. These findings align with the findings of Bhattacharya et al. [29].

Fig. 7 depicts the absorption spectra of the prepared thin films. It shows that the samples had the highest absorption at a wavelength of 300 nm. It was noted that as the wavelength increased, the absorption reduced in all samples. This is attributed to the incident light possessing an energy below the bandgap, thus failing to meet the absorption requirements. Additionally, it was noted that the basic absorption edge of TiO_2:CdS changed towards longer wavelengths after the inclusion of CdS into TiO_2. The TiO_2:CdS films had strong UV absorption while showing little absorption of visible light [30]. The absorbance of all the generated samples was similar and showed a little reduction as the CdS concentrations increased. These findings align with the outcomes of the study conducted by Kripal et al. [31].

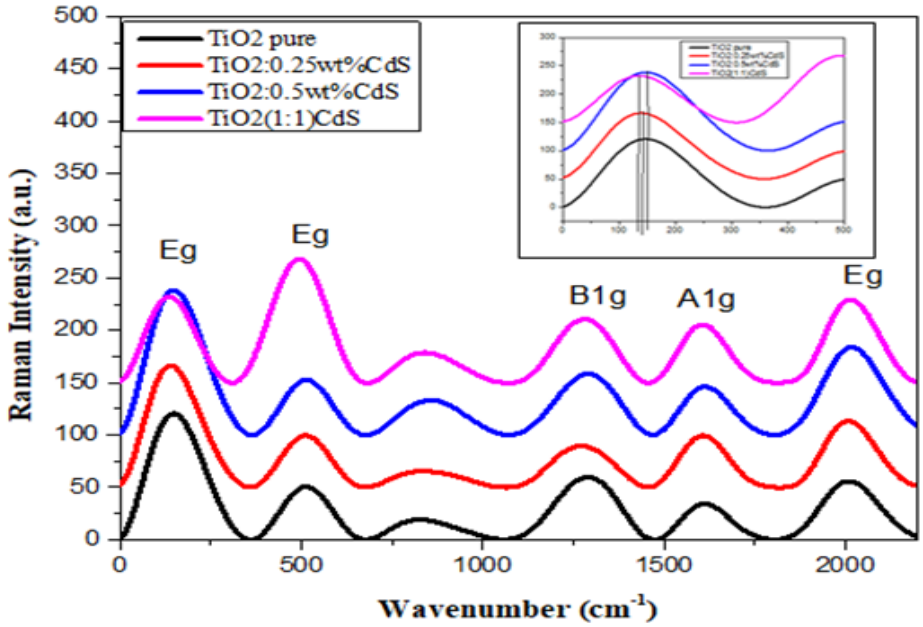

Figure 6: Raman spectroscopy of TiO_2 and TiO_2:CdS thin films.

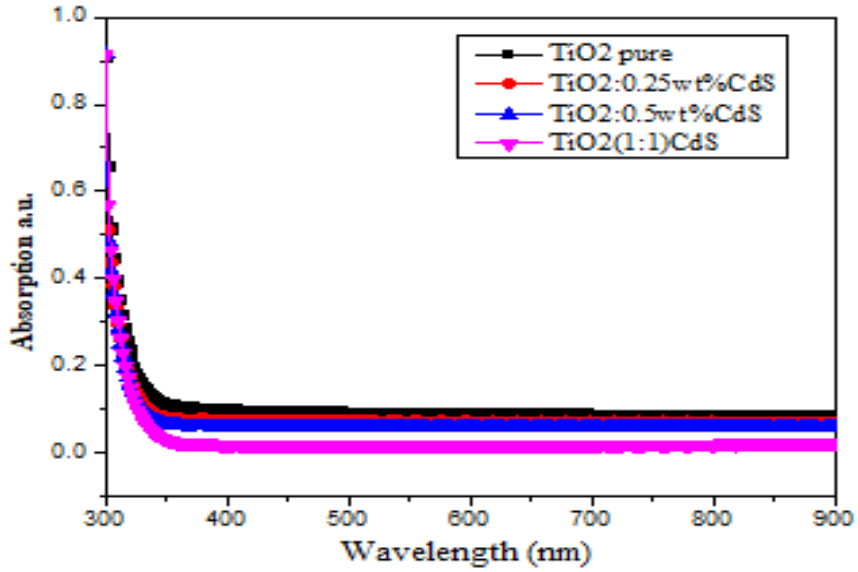

Figure 7: The absorption of Au/TiO_2: CdS thin films.

The Tauc relation [32] was used to calculate the energy gap (E_g):

$$(\alpha h\nu)^{1/n} = A(h\nu - E_g) \quad \textbf{(12)}$$

where α is the optical absorption coefficient of the material, hν is the energy of the incident photon, A is a constant depends on the transition probability and the density of cases, and n depends on the nature of the electronic transition in the material.

The energy gap of all produced thin films was determined by plotting $(\alpha h\nu)^2$ as a function of (hυ), as shown in Fig. 8. The energy gap values for the thin films were obtained by extending the straight line of the curve and finding its intersection with the x-axis. Energy gap of pure TiO_2 was determined to be 3.5 eV, indicating that the energy gap is direct and consistent with the findings of previous investigations [33]. The results showed the energy gap grew from 3.5 to 3.68 eV with increasing CdS concentration. As the CdS concentration increases, localized levels form within the energy gap, leading to an increase in the energy gap. This, in turn, results in a decrease in electronic transfer [34].

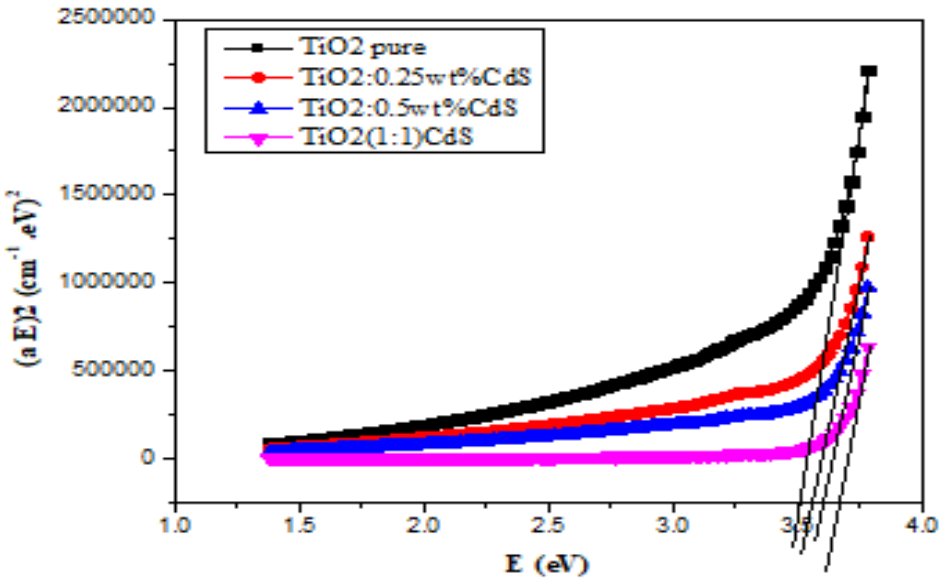

Figure 8: Tauc plots to calculate the energy gap of Au/ TiO_2: CdS thin films.

This study investigated the photocatalytic elimination and decomposition of dye pollutants using Au/TiO_2:(0, 0.25, 0.5, and 1:1) wt% CdS thin films with 5 mg/L concentration MB dye. The prepared samples were immersed in a solution of MB dye and remained in darkness for the first 10 minutes to assess the dye's ability to be absorbed. Subsequently, light illumined the inside the photocatalytic reactor for one hour, after which the photodegradation process was examined. In summary, the decrease in dye concentration in the absence of light indicated that the dye molecules were physically transferred from the solution to the surface of the adsorbent.

When semiconductors are exposed to light, they create photo charge carriers, namely photoelectric electrons in the conduction band and photo holes in the valence band. These carriers then form superoxide and hydroxyl radicals, respectively. In summary, when light generates holes and electrons, they combine with water and dissolve oxygen to produce a hydroxyl radical (•OH) and a superoxide radical ($O_2^{\bullet-}$). The highly reactive species (•OH and $O_2^{\bullet-}$) engage in numerous interactions with organic contaminants in the liquid medium to break down the pollutants [35, 36].

Fig. 9 shows the percentage ratio between the final dye concentration C_i and the initial concentration C_o versus time. In the absence of absorbent photocatalytic materials (thin films) and with the presence of lighting (UV light), it was observed that there was no change in the concentration of the MB dye when exposed to ultraviolet radiation with the exposure time. After introducing the prepared samples TiO_2 and TiO_2:CdS into the dye solution, a change in the concentration of MB dye was observed under light conditions in a range of change ranging from 0.002 to 0.008. When thin semiconductor films are illuminated, an electron gap is formed. These electrons also interact with water molecules to produce superoxide and hydroxyl radicals, which lead to the decomposition of dye molecules [37]. The results showed that when CdS was added to TiO_2, it can play a dominant role as a light harvester, and CdS mainly acts as a cocatalyst to enhance charge separation [38]. Fig. 10 explains that the degradation of the dye increases with increasing concentrations of CdS, as the lowest degradation was for the pure TiO_2 sample and the highest degradation was for the TiO_2:CdS(1:1) sample. The efficiency of degradation dye was calculated from Eq.(13) [39]:

$$\text{Degradadtion} = \left(\frac{C_o - C_i}{C_o}\right) \times 100\% \quad \textbf{(13)}$$

The optimal photocatalytic performance for methyl blue dye degradation was observed with the TiO_2:CdS (1:1) film, reaching an efficiency of 1.41%. Conversely, the pure TiO_2 sample exhibited the lowest decomposition efficiency, at 0.88% (see Table 3). Also, Fig. 10 indicates that the degradation efficiency percentage increased with the increase in CdS concentration. The reason can be referred to the presence of CdS, as it which improved the bandgap and thus increases the decomposition efficiency [39].

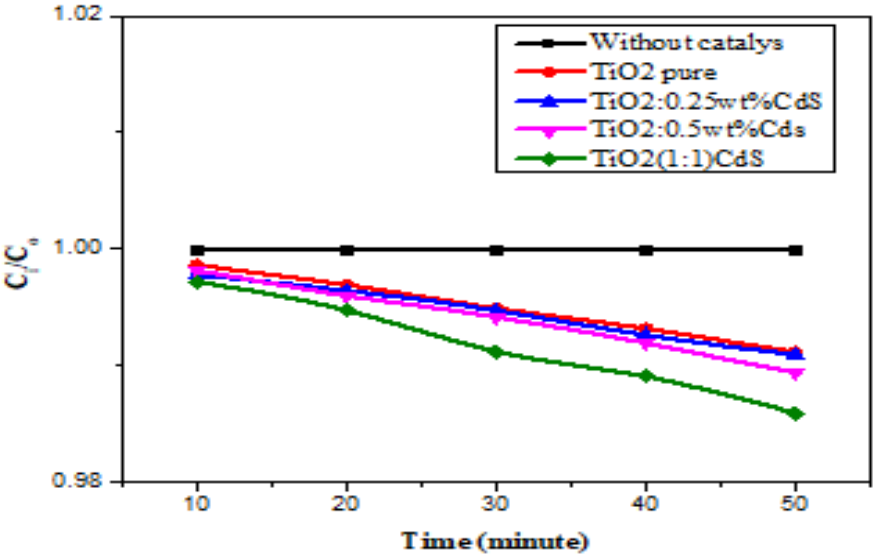

Figure 9: Photocatalytic degradation for Au/TiO_2:CdS thin films of MB dye.

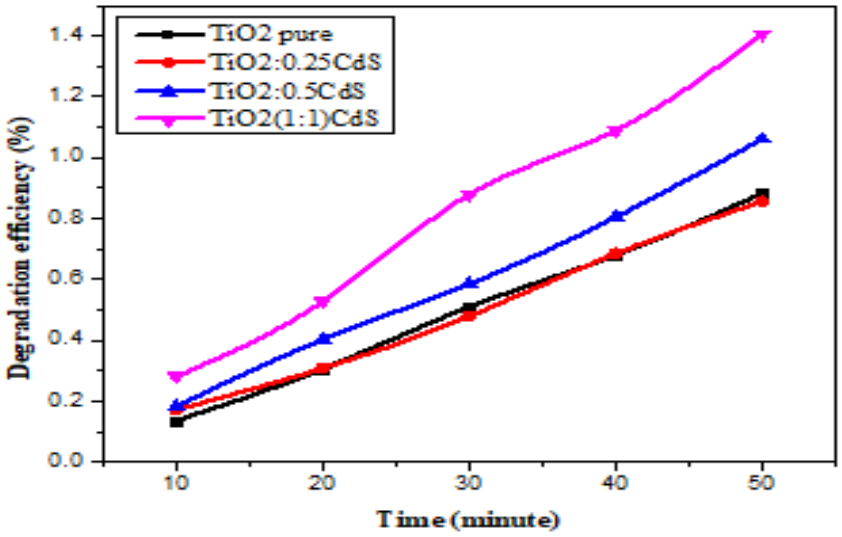

Figure 10: The Degradation efficiency% of Au/TiO_2:CdS thin films for MB dye.

Table 3: The high efficiency for Au/TiO_2: CdS thin films degradation of MB dye.

Samples	degradation efficiency %	Rate constant (k) E-4 $(min)^{-1}$
TiO_2 pure	0.883152	1.87772
TiO_2:0.25CdS	0.855278	1.75433
TiO_2:0.5CdS	1.060717	2.17145
TiO_2:CdS(1:1)	1.405975	2.8357

Using the pseudo-first-order reaction equation ($k=slope=\ln(C_i/C_o)/t$) [40], the photocatalytic reaction rate constant (k) was calculated from the plots shown in Fig. 11 and Table 3. Furthermore, Fig. 12 displays the k values of the as-prepared samples to illustrate how the photocatalytic reaction rate constant k varies with the increased content of CdS. The charts demonstrated that when CdS was added, k increased. Excluding the 0.25% CdS sample, the observed trend indicates that the photocatalytic rate constant generally improves with increasing CdS content. The behavior of the dissolution coefficient can be elucidated through three distinct mechanisms:

1. As CdS concentrations rise, so does the effectiveness of UV absorption, which raises the e/h pair generation.
2. Increasing the CdS concentration leads to a greater availability of the bulk material, consequently accelerating the adsorption process.
3. It was also noted that the more layers there are, the rougher the surface becomes, increasing the dye breakdown efficiency. Compared to TiO_2 films with a smoother surface, those with a rougher surface have a greater breakdown efficiency. Several publications have shown that the porous surface enhances the active surface sites, which in turn boosts the films' catalytic activity [41].

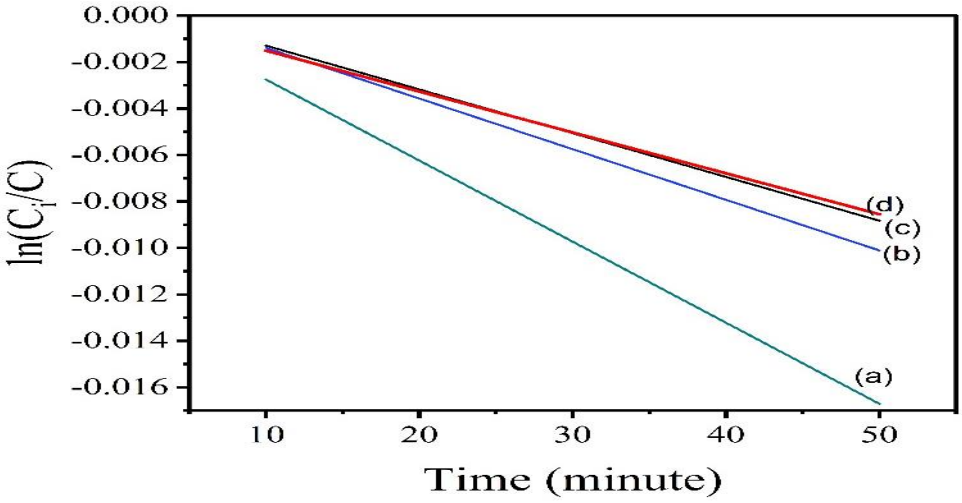

Figure 11: The photocatalytic reaction ln (Ci/Co) against exposure time of Au/TiO_2: CdS thin films as degradation of MB dye, (a) TiO_2:CdS(1:1), (b) at 0. 5wt%CdS, (c)pure TiO_2, (d) at 0.25wt%CdS.

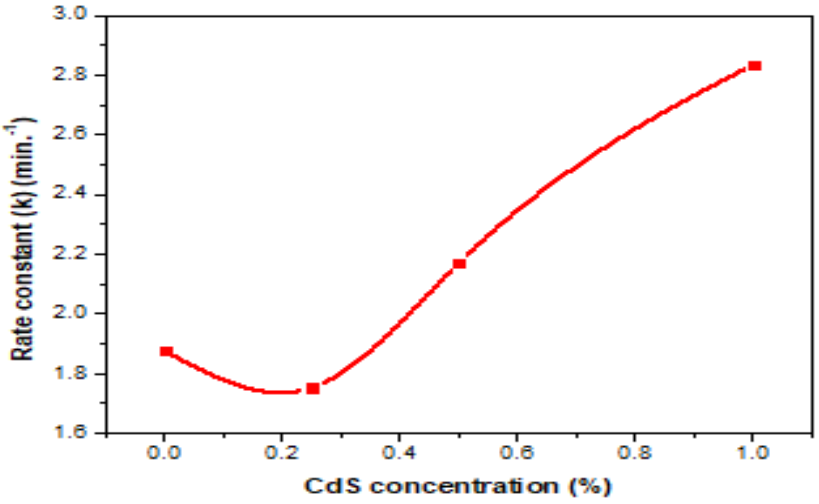

Figure 12: Rate constant(k) of Au/ TiO_2: CdS thin films vs. CdS content.

3. Conclusions

In this work, Au/TiO_2:CdS thin films of TiO_2:CdS, TiO_2:0.25%CdS, and TiO_2:0.5%CdS were deposited on glass substrates using the sol-gel and the dipping methods. The results of XRD revealed that the films are polycrystalline with a cubic phase of TiO_2 structure and TiO_2:CdS structure; also, the crystalline size increased with increasing CdS content, except for the sample TiO_2 (1:1)CdS where the crystalline size decreased. The microstructure parameters of TiO_2:CdS thin films, such as macrostrain and dislocation density, were calculated, and the results showed random values. AFM analysis revealed a general trend of decreasing grain size and increasing surface roughness with elevated CdS concentration. An exception to this trend was observed in the TiO_2(1:1)CdS sample, where these parameters remained relatively stable. FESEM results revealed that the particle size decreased with increasing CdS concentration. Raman spectroscopy revealed the emergence of TiO_2 peaks, alongside a discernible blue shift, following the incorporation of CdS into the TiO_2 matrix. The optical properties revealed that absorption decreased and the band gap increased with increasing CdS concentration. The thin films of TiO_2:CdS showed that the decomposition efficiency and the rate constant increased with increasing CdS concentration; therefore, adding CdS to the TiO_2 enhances the degradation efficiency of TiO_2 at the ratios of added CdS.

Acknowledgements

The authors would like to thank the University of Baghdad College of Science for Women, Department of Physics, for their assistance in carrying out this work, as well as the Scientific Research Commission, Ministry of Higher Education, Scientific Research, Baghdad, Iraq.

Conflict of Interest

Authors declare that they have no conflict of interest.

References

1. D. Tryk, Electr. Soci., **68**, 4795, (2024). https://doi.org/10.1149/MA2024-02684795mtgabs.
2. S. Linic, P. Christopher, and D.B. Ingram, Nat. Mater., **10**, 911, (2011). https://doi.org/10.1038/NMAT3151.
3. N. S. Lewis, Nature, **414**, 589, (2001). https://doi.org/11.1116/6.0011435.
4. C. G. Silva, R. Juárez, T. Marino, R. Molinari, and H. García, J. Am. Chem. Soc., **133**(3), 595, (2011). https://doi.org/10.1021/ja1086358.

5. A. Bumajdad and M. Madkour, Phys. Chem. Chem. Phys., **16**, 7146, (2014). https://doi.org/10.1039/C3CP54411G.
6. H. Akazawa, J. of Vacu. Scie. & Techn., A, **40**, 013407, (2022). https://doi.org/10.1116/6.0001434.
7. Z. Shi, J. Liu, H. Lan, X. Li, B. Zhu, and J. Yang, J. Mater. Sci. Mater. Electron, **30**(19), 17682, (2019). https://doi.org/10.1007/s10854-019-02118-x.
8. Q. Shen, J. Xue, H. Zhao, M. Shao, X. Liu, and H. Jia, J. Alloys Compd., **695**, 1080, (2017). https://doi.org/10.1016/j.jallcom.2016.10.233.
9. M. Golmohammadi, M. Hassankiadeh, and L. Zhang, L. Cera. Inter., **47**(20), 29303, (2021). https://doi.org/10.1016/j.ceramint.2021.07.095.
10. T.-W. Liao, S. Verbruggen, N. Claes, A. Yadav, D. Grandjean, S. Bals, and P. Lievens, Nanomaterial, **8**(1), 30, (2018). https://doi.org/10.3390/nano8010030.
11. S. Veziroglu, K. Röder, O. Gronenberg, A. Vahl, O. Polonskyi, T. Strunskus, G. Rubahn, L. Kienle, and J. Adam, Nanoscale, **11**, 9840, (2019). https://doi.org/10.1039/C9NR01208G.
12. S. W. Verbruggen, M. Keulemans, B. Goris, N. Blommaerts, S. Bals, J.A. Martens, and S. Lenaerts, Appl. Catal. B Environ, **188**, 147, (2016). https://doi.org/10.1016/j.apcatb.2016.02.002.
13. J. Chang, C. Saint, C. Chow, D. Bahnemann, and M. Chong, M. Inter. Mate. Revi., **69**(7-8), 337, (2024). https://doi.org/10.1177/09506608241280421.
14. A. Al-Taie and H. Dah, Baghdad Sci. J., **14**(3), 582, (2017). http://dx.doi.org/10.21123/bsj.2017.14.3.0582.
15. S. A. Mousa, S. Tareq, and E. A. Muhammed, Baghdad Sci J., **18**(4), 1261, (2021). https://doi.org/10.21123/bsj.2021.18.4.1261.
16. N. Qutub, P. Singh, S. abir, S. Sagadevan, and W. Oh. Scie. Rep., **12**(1), 5759, (2022). https://doi.org/10.1038/s41598-022-09479-0.
17. S. Pandeya, R. Ding, Y. Ma, X. Han, M. Gui, and P. Mulmi, J. of Envi. Chem. Engi., **12**(3), 112521, (2024). https://doi.org/10.1016/j.jece.2024.112521.
18. E. Mittemeijer and P. Scardi. Diffraction analysis of the microstructure of materials, 1st ed. Vol. 68, Springer Berlin, Heidelberg (2004). https://doi.org/10.1007/978-3-662-06723-9.
19. S. Sharma, N. Kumar, B. Mari, N. Chauhan, A. Mittal, S. Maken, and K. Kumari, K. Inorg. Chem. Commu., **125**, 108418, (2021). https://doi.org/10.1016/j.inoche.2020.108418.
20. S. Sharma, A. Mittal, N. Chauhan, S. Saini, J. Yadav, M. Kushwaha, and N. Kumar, J. of Phys. and Chem. of Solid, **162**, 110510, (2022). https://doi.org/10.1016/j.jpcs.2021.110510.
21. J. Aoudjt, A. Queirós, D. Castro, N. Zioui, Nanomaterials, **15**(5), 358, (2025). https://doi.org/10.3390/nano15050358.
22. S. Al-Jawad, Mate. Scie. in Semi. Proce., **67**, 75, (2017). https://doi.org/10.1016/j.mssp.2017.05.014.
23. M. Darrudi, H. Tavakol, and M. Momeni, Inte. J. of Hydr. Energy, **48**(9), 3495, (2023). https://doi.org/10.1016/j.ijhydene.2022.10.145.
24. R. Zhou, Q. Zhang, E. Uchaker, J. Lan, M. Yin, and G. Cao, J. of Mate. Chem. A, **2**, 2517, (2014). https://pubs.rsc.org/en/content/articlelanding/2014/ta.
25. A. Cerdán-Pasarán, T. López-Luke, I. Zarazúa, E. De la Rosa, R. Fuentes-Ramírez, K. C. Sanal, and A. Alatorre-Ordaz, J. of Appli. Electr., **49**, 475, (2019). https://link.springer.com/article/10.1007/s10800-019-01299-x.
26. M. Revathi and A. Jeyakumari, J. of Mate. Scie.: Mate. in Elect., **32**, 11921, (2021). https://link.springer.com/article/10.1007/s10854-021-05822-9.
27. B. Khosravi and R. Gordon, J. of Phys. Chem. C, **128**(36), 15048, (2024). https://doi.org/10.1021/acs.jpcc.4c03536.
28. M. Salis, P. Ricci, and A. Anedda, J. of Raman Spectr., **40**, 64, (2009). https://doi.org/10.1002/jrs.2076.
29. S. Bhattacharya, A. Pal, A. Jana, and J. Datta, J. of Mate. Science: Mate. in Elect., **27**, 12438, (2016). https://link.springer.com/article/10.1007/s10854-016-5298-3.
30. V. Cáceres, C. Nieves, C. Plaza-Rivera, E. Pacheco, A. Reyes-Diaz, and A. Rúa, Instr. Scie. & Techn., **1**, (2024). https://doi.org/10.1080/10739149.2024.2431967.
31. R. Kripal, G. Vaish, and U. Tripathi, J. of Electr. Mater., **48**, 1545, (2019). https://link.springer.com/article/10.1007/s11664-018-06894-w.
32. C. Kittel, *Introduction to solid state physics*. 8th ed. John Wiley & Sons Inc. (2021). https://doi.org/10.1005/jrs.2075.
33. M. Mithun, A. Sayed, and I. Rahaman, Proceedings of Engi. and Techn. Inno., **19**, 45, (2021). https://doi.org/10.46604/peti.2021.7712.
34. A. H. Kahdim, N. B. Hasan, and H. B. Hasan, Inter. J. of Adva. Engi., Manag. and Scie., **4**(3), 189, (2018). 10.22161/ijaems.4.3.9.
35. R. Tang, C. Dai, C. Li, and C. Wang, J. of Chem., **2017**, 8404965, (2017). https://doi.org/10.1155/2017/8404965.
36. J. Kim, S. Kang, S. Lee, J. Ok, Y. Kim, and A. Kim, Adva. Funct. Mate., **30**(50), 2003862, (2020). https://doi.org/10.1002/adfm.202003862.

37. S. Khan, T. Noor, N. Iqbal, and L. Yaqoob, ACS Omega, **9**(20), 21751, (2024). https://doi.org/10.1021/acsomega.4c00887.
38. M. Elangovan, S. Bharathaiyengar, and J. P. Ettiyappan, Envi. Scie. and Pollution Rese., **28**, 18186, (2021). 10.1007/s11356-020-11538-w.
39. Y. Liang, J. Sun, Y. Lu, M. Xiu, J. Zhang, and Y. Huang, J. of Alloys and Comp., **980**, 173629, (2024). https://doi.org/10.1016/j.jallcom.2024.173629.
40. N. Ghasem, *Computer Methods in Chemical Engineering,* 2nd Edition, (2023, CRC Press), P. 490, https://doi.org/10.1201/9781003167365.
41. C. Aprile, A. Corma, and H. Garcia, Phys. Chemistry, **10**(6), 769, (2008). https://doi.org/10.1039/B712168G.

تحضير وتوصيف غشاء رقيق من $Au/TiO_2:CdS$ كعامل تحفيز ضوئي لتحلل صبغة بروميد الميثيل في الماء

زينب قاسم محمد[1] ومهدي محمود مطر[2] وسعاد غفوري خليل[1]
[1]قسم الفيزياء، كلية العلوم للبنات، جامعة بغداد، بغداد، العراق
[2]هيئة البحث العلمي، وزارة التعليم العالي والبحث العالي، بغداد، العراق

الخلاصة

تم تصنيع نانومركبات رقيقة من الذهب/أكسيد التيتانيوم: كبريتيد الكادميوم ($Au/TiO_2:CdS$) كمحفزات ضوئية باستخدام تقنية السول-جل، في هذا العمل، وترسيبها على ركائز زجاجية باستخدام طريقة الغمس لتحلل صبغة الميثيلين الأزرق (MB) في الماء. تم تطعيم كبريتيد الكادميوم بثاني أكسيد التيتانيوم (TiO_2) بنسب 1:1، و0.25، و0.5% وزناً. تم توصيف الأغشية الرقيقة من الذهب/تيو$_2$: كبريتيد الكادميوم باستخدام حيود الأشعة السينية (XRD)، ومجهر القوة الذرية (AFM)، وطيف رامان، ومجهر مسح الإلكترونات بتأثير المجال (FESEM)، وطيف الأشعة فوق البنفسجية-المرئية. أظهرت نتائج حيود الأشعة السينية أن الطور الناتج من ثاني أكسيد التيتانيوم: كبريتيد الكادميوم كان مكعباً. كما أظهرت نتائج مجهر القوة الذرية أن توزيع أحجام الحبيبات ازداد مع زيادة تركيز كبريتيد الكادميوم، وكذلك خشونة السطح ومتوسط التربيع. أشارت نتائج FESEM إلى أن حجم الجسيمات انخفض من 58.68 نانومتر إلى 22.24 نانومتر مع زيادة تركيز CdS. وكشفت مطيافية رامان أن قمم TiO_2 تظهر فقط عند 1300 سم$^{-1}$ (B1g)، و1600 سم$^{-1}$ (A1g)، و2000 سم$^{-1}$ (Eg). وقد تحسنت الخصائص البصرية بعد إضافة CdS. وقد تم دراسة التحلل الضوئي لأغشية Au/TiO_2 الرقيقة من CdS عن طريق تحلل صبغة MB في الماء تحت التعرض للأشعة فوق البنفسجية. وأظهرت النتائج أداءً ضوئيًا ممتازًا بعد إضافة CdS.

الكلمات المفتاحية: غشاء رقيق من Au/TiO_2: CdS، خواص تركيبية، تحفيز ضوئي، مقياس رامان الطيفي، صبغة الثيل الاخضر.